Volume 10 | Number 23 | 7 December 2023

10 YEARS ANNIVERSARY

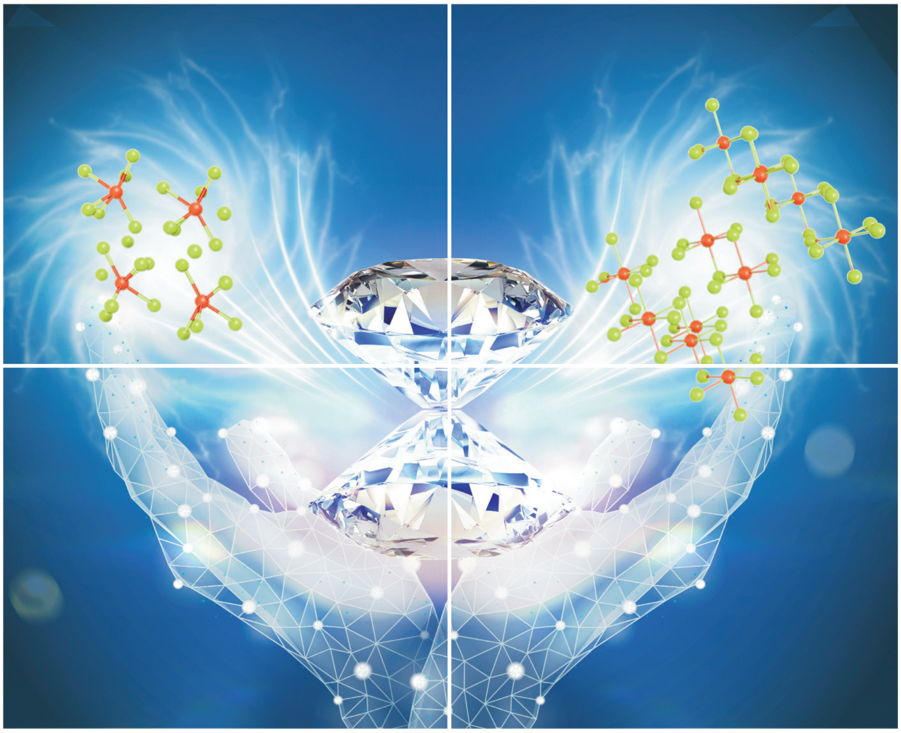

INORGANIC CHEMISTRY FRONTIERS

CCS 中国化学会 CHINESE CHEMICAL SOCIETY

PEKING UNIVERSITY 1898

ROYAL SOCIETY OF CHEMISTRY

rsc.li/frontiers-inorganic

INORGANIC CHEMISTRY
FRONTIERS

CHINESE CHEMICAL SOCIETY
ROYAL SOCIETY OF CHEMISTRY

RESEARCH ARTICLE

View Article Online
View Journal | View Issue

Cite this: *Inorg. Chem. Front.*, 2023, **10**, 6849

Pressure-driven structural and electronic transitions in a quasimolecular layered compound of antimony triiodide†

Meiling Hong,[a] Lidong Dai, *[a] Haiying Hu, *[a] Xinyu Zhang,[a,b] Chuang Li,[a,b] Xiaolei Feng,[c] Shidong Yu, [d] Limin Zhang,[a,b] Zhongying Mi[a] and Sivakumar Aswathappa[a]

Quasimolecular layered metal triiodides MI_3 (M = Sb and Bi) hold immense promise in applications of solid-state batteries, radiation detectors, and photocatalysts owing to their favorable physicochemical properties. As a representative MI_3 compound, antimony triiodide (SbI_3) exhibits high-pressure phase stability beyond 16.0 GPa and its electrical transport behaviors remain largely unknown. In this study, we systemically investigated the structural and electronic transitions of SbI_3 during compression and decompression under different hydrostatic environments using synchrotron X-ray diffraction, Raman spectroscopy, electrical conductivity, and first-principles theoretical calculations. During compression, SbI_3 endured two isostructural phase transitions (IPTs) at the respective pressures of 3.4 GPa and 10.3 GPa stemming from the prominent compression of the *c*-axis and Sb–I bond. Upon further compression to 32.3 GPa, an electronic transition from the semiconductor to metal occurred in SbI_3 under non-hydrostatic conditions, which was possibly associated with the rhombohedral ($R\bar{3}$)-to-monoclinic ($C2/m$) structural transformation. Under hydrostatic conditions, a considerable pressure hysteresis of ~5.0 GPa was detected for the emergence of metallization owing to the faint deviatoric stress. During decompression, the phase transition of SbI_3 was revealed to be irreversible under different hydrostatic environments, which was probably caused by the huge kinetic barrier for the continuous high-pressure structural transitions. Our high-pressure study on SbI_3 offers an in-depth insight into the correlations between crystalline and electronic structures, and may facilitate the application of quasimolecular layered crystals in optoelectronic devices.

Received 15th June 2023,
Accepted 23rd August 2023

DOI: 10.1039/d3qi01126g

rsc.li/frontiers-inorganic

Introduction

The VA group metal triiodides MI_3 (M = Sb and Bi), a class of novel two-dimensional (2D) compounds, have attracted much interest owing to their unique physicochemical properties and versatile applications.[1,2] A distinctive member in MI_3 materials, SbI_3 possesses excellent optical and electrical properties, and thus emerges as a promising candidate for solid-state batteries, radiation detectors, and photocatalysts.[2–6] SbI_3 forms a quasimolecular layered crystal, where each layer is constituted by an I–Sb–I sandwich *via* strong covalent–ionic bonds, and the adjacent layers are piled up along the *c*-axis direction by weak van der Waals interactions.[7–9] At ambient conditions, SbI_3 is a wide bandgap semiconductor (~2.2 eV) and crystallizes into a rhombohedral system with a space group of $R\bar{3}$.[4,10,11]

Pressure is an efficient and powerful tool for modulating the crystalline and electronic structures of 2D materials, giving rise to the emergence of structural and electronic transitions under high pressure.[12–16] The high-pressure structural stability and electrical transport behavior of antimony triiodide were explored using synchrotron X-ray diffraction, Raman spectroscopy, and first-principles theoretical calculations in previous studies.[9,17,18] However, there exist some unresolved issues concerning the phase stability beyond 16.0 GPa and the deficiency of experimental evidences for metallization in SbI_3. Anderson *et al.* (1998) deduced that SbI_3 experienced a

---

[a] *Key Laboratory of High-Temperature and High-Pressure Study of the Earth's Interior, Institute of Geochemistry, Chinese Academy of Sciences, Guiyang, Guizhou 550081, China. E-mail: dailidong@vip.gyig.ac.cn, huhaiying@vip.gyig.ac.cn*
[b] *University of Chinese Academy of Sciences, Beijing 100049, China*
[c] *School of Materials Science and Engineering, Nanyang Technological University, 50 Nanyang Avenue, 639798, Singapore*
[d] *Asian School of the Environment, Nanyang Technological University, 50 Nanyang Avenue, 639798, Singapore*

† Electronic supplementary information (ESI) available. CCDC 2288996–2288998. For ESI and crystallographic data in CIF or other electronic format see DOI: https://doi.org/10.1039/d3qi01126g

sequence of reversible phase transitions at 0.3, 0.8, and 4.9 GPa from the evolution of high-pressure Raman spectra. As the pressure increased to 8.3 GPa, an irreversible structural transformation occurred and the high-pressure phase remained stable up to the highest experimental pressure of ∼16.0 GPa.[17] Subsequent synchrotron X-ray diffraction and Raman scattering measurements on SbI_3 showed an IPT associated with the molecular-to-ionic crystal switching, and SbI_3 further transformed into the monoclinic phase ($P2_1/c$) above 4.0 GPa.[9] More recently, the rhombohedral ($R\bar{3}$)-to-monoclinic ($P2_1/c$) structural transition was theoretically predicted at ∼6.5 GPa based on the low enthalpy criterion.[18] Furthermore, the bandgap of the $P2_1/c$ structural phase significantly decreased with the rise of pressure and ultimately closed at ∼55.0 GPa, implying the occurrence of metallization. Although theoretical calculation results suggested the presence of metallization in pressurized SbI_3, the experimental evidences of an electronic transition under high pressure have remained scarce until now.[18] Meanwhile, when the pressure is higher than 16.0 GPa, the phase stability of SbI_3 is ambiguous.

No pressure medium (PM) was employed in previous high-pressure synchrotron X-ray diffraction and Raman scattering measurements due to the fact that SbI_3 possibly undergoes a chemical reaction with potassium bromide (KBr) or dissolves into the mixture of methanol and ethanol (4 : 1 volume ratio).[9,17] Different from potassium bromide and the mixture of methanol and ethanol, noble gases (*e.g.*, helium, argon, neon, nitrogen, *etc.*) were considered as a better choice due to their stable physicochemical properties and high hydrostaticity, which has been reported to prominently influence the structural properties of 2D materials under high pressure.[12–16,19–22] As for SbI_3, the related research on the high-pressure structural behaviors under both non-hydrostatic and hydrostatic conditions is still lacking.

In this work, SbI_3 endured the pressure-induced IPTs and metallization under different hydrostatic environments up to 50.0 GPa using a diamond anvil cell (DAC) coupled with synchrotron X-ray diffraction, Raman spectroscopy, alternating current impedance spectroscopy and first-principles theoretical calculations. The two phase transitions and metallization of SbI_3 during compression and the irreversibility of phase transformation during decompression are discussed in detail.

Experimental section

Sample preparation and characterization

High-purity (99.99%) polycrystalline SbI_3 powders with red surface color were commercially purchased as the starting materials. The chemical composition and crystalline structure of the initial specimen were determined by energy dispersive X-ray spectroscopy (EDS) and an Empyrean-type X-ray powder diffractometer with copper Kα radiation (λ = 1.5406 Å). The EDS spectrum revealed the characteristic peaks of antimony and iodine. Furthermore, the atomic ratio of antimony and iodine was determined as 1 : 2.88, which is close to the chemical formula of SbI_3 (see Fig. 1a). As shown in Fig. 1b, the Rietveld analysis results of the X-ray diffraction (XRD) pattern can be well-indexed to the rhombohedral SbI_3 system with a space group of $R\bar{3}$ (JCPDS no. 74-0456), yielding the lattice parameters of $a = b = 7.495 \pm 0.001$ Å, $c = 20.957 \pm 0.004$ Å, $\alpha = \beta = 90°$, $\gamma = 120°$ and $V = 1019.55 \pm 0.29$ Å^3 at ambient conditions. Furthermore, our acquired lattice parameters of SbI_3 are in good agreement with prior results.[6,23,24]

High-pressure Raman spectroscopy, electrical conductivity and synchrotron X-ray diffraction experiments

A symmetrical DAC mounted with 200 μm-diameter culets was utilized for high-pressure Raman scattering, electrical conductivity and synchrotron X-ray diffraction experiments of SbI_3. In Raman spectroscopy measurements, the experimental sample and ruby acting as the pressure calibration were sealed into a 100 μm-diameter sample chamber. Two groups of Raman scattering experiments were implemented, one with helium as the PM to reach hydrostatic condition and the absence of PM in another run for non-hydrostatic condition. Meanwhile, the hydrostaticity under different hydrostatic environments was checked by loading several ruby balls in the center and edge of the sample chamber. From Fig. S1,† with the rise of pressure, the deviatoric stress increased considerably under non-hydrostatic condition, whereas a relatively feeble pressure-dependent deviatoric stress was detected under hydrostatic condition, which verified the excellent hydrostaticity using helium as the pressure medium. Raman spectra of SbI_3 were recorded by a Renishaw 2000 micro confocal Raman spectrometer with the diode laser (λ = 785 nm) as an excitation source in the backscattering geometry. As for the electrical conductivity measurements, the insulation powder constituted by epoxy and boron nitride was firmly compressed into a 180 μm-diameter central hole. Afterwards, another 100 μm-diameter hole was laser-drilled as the insulating sample chamber, and the remaining segment of the gasket was uniformly coated by the insulation cement. Double-parallel-plate electrodes were integrated onto the upper and lower sections of the sample chamber for elec-

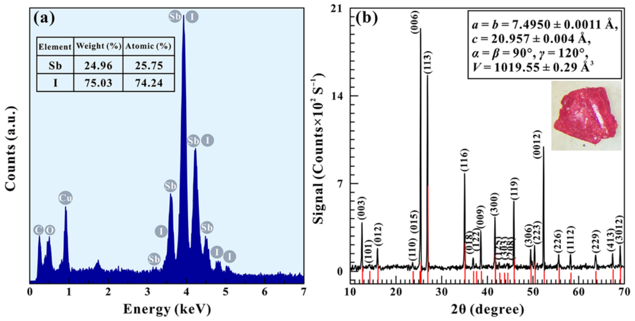

Fig. 1 (a) The EDS spectrum of the starting sample. (b) Representative XRD pattern for the initial specimen at ambient conditions. Therein, the red vertical lines are the standardized peak positions for the rhombohedral SbI_3 system with a space group of $R\bar{3}$. Inset: Optical microscope photograph and some crucial crystalline parameters for the pristine sample.

trical conductivity measurements. No pressure medium was applied in the electrical conductivity experiments to provide the non-hydrostatic condition and efficiently avoid introducing additional impurities. In the case of the employment of extra pressure medium during high-pressure electrical conductivity experiment, it will seriously affect the precision of experimental results. The complex impedance spectra of the sample were measured by a Solartron-1260 impedance/gain phase analyzer coupled with a Solartron-1296 dielectric interface over the frequency range of 10^{-1}–10^{7} Hz at an applied voltage of 3.0 V. In variable-temperature electrical conductivity experiments, a low temperature was created by liquid nitrogen and the temperature was directly measured with a K-type thermocouple adhered to the side of a diamond anvil. The angle-dispersive synchrotron X-ray diffraction experiments were performed at the 4W2 beamline of the Beijing Synchrotron Radiation Facility (BSRF), Beijing, China. The incident X-ray wavelength is 0.6199 Å. The collected XRD patterns of SbI_3 were processed by the Rietveld refinement using the General Structure Analysis System (GSAS) software package to resolve the structures and retrieve the lattice parameters.[25] Moreover, experimental samples with a similar grain size of 1–3 μm were utilized in high-pressure Raman scattering, electrical conductivity and synchrotron X-ray diffraction experiments under different hydrostatic environments to avoid the possible influence of grain size on the vibrational property, crystalline structure and electrical transport behavior under high pressure. More details of the experimental procedures referred to our previous works.[12–16,22]

Computational details

First-principles theoretical calculations of SbI_3 were performed with density functional theory (DFT) as implemented in the Vienna *ab initio* Simulation Package (VASP) code at the National Supercomputing Centre (NSCC), Singapore.[26] The strongly constrained and approximately normed (SCAN) meta-GGA functional and projector augmented wave (PAW) theory was employed in the geometric optimization and electronic band structure calculations.[27–29] In the PAW potentials, the $5s^25p^3$ and $5s^25p^5$ valence electrons were considered for Sb and I, respectively. The maximum kinetic energy cut-off for plane wave expansions of the wavefunctions was set to 520 eV. The Monkhorst–Pack grid with a spacing of 0.5 $Å^{-1}$ was utilized in the integration of the DFT total energies. The crystalline parameters and ionic positions were fully relaxed with the residual forces on the atoms at less than 10 meV $Å^{-1}$.

Results and discussion

High-pressure Raman spectra of SbI_3

Fig. 2a–c are the representative high-pressure Raman spectra of SbI_3 under the conditions of 0.4–48.1 GPa and atmospheric temperature. At 0.4 GPa, four prominent Raman peaks at 41.2, 62.7, 134.6 and 156.9 cm^{-1} were identified within the wavenumber range of 30–300 cm^{-1}, which can be assigned as the T_z, v_4, v_1 and v_3 modes of SbI_3, respectively. Herein, the v_1 and v_3 modes are related to the Sb–I stretching vibration and the v_4 mode arises from the I–Sb–I bending vibration. Meanwhile, the T_z mode derives from the optical translation.[6–9] Furthermore, our observed Raman peaks of SbI_3 match well with prior results.[6–9]

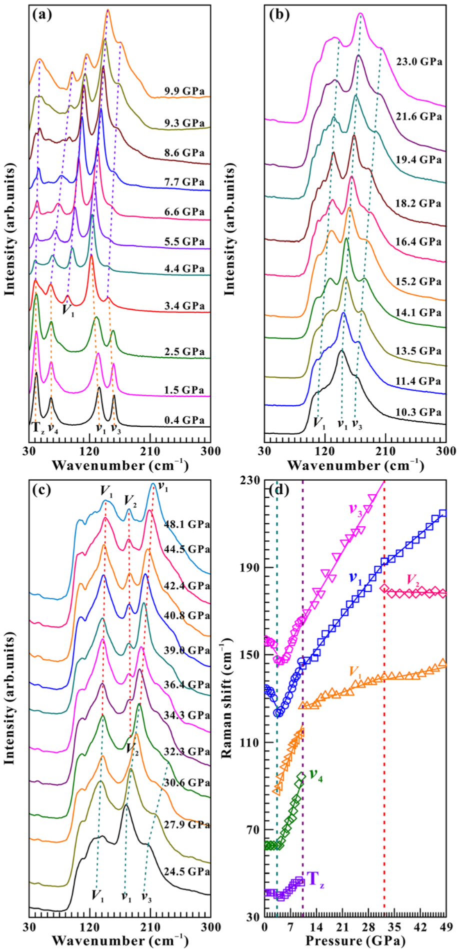

Fig. 2 High-pressure Raman spectroscopy of SbI_3 under non-hydrostatic condition within the pressure range of (a) 0.4–9.9 GPa, (b) 10.3–23.0 GPa, and (c) 24.5–48.1 GPa. (d) The pressure dependence of Raman shift for SbI_3 during compression. Errors in both Raman shifts and pressures are within the size of the symbols.

Within the pressure range of 0.4–2.5 GPa, the Raman peaks of SbI_3 exhibited red shifts with the application of pressure, indicating the structural instability or phase transition.[9,17] When the pressure elevated to 3.4 GPa, a new Raman peak at 87.5 cm^{-1} (defined as the V_1 mode) emerged and its Raman peak intensity enhanced appreciably under compression. Beyond 3.4 GPa, all of these Raman peaks of the sample shifted toward higher wavenumbers with the rise of pressure. Concurrently, the v_1 Raman peak became dominant, whereas the T_z, v_4 and v_3 Raman peaks tended to be weakened and broadened significantly. At 10.3 GPa, both T_z and v_4 Raman peaks disappeared, accompanied by a substantial broadening of the remaining Raman peaks. Upon further pressurization above 10.3 GPa, three predominant Raman peaks of V_1, v_1 and v_3 continuously shifted toward higher wavenumbers. As the pressure approached to 32.3 GPa, the v_3 Raman peak became invisible. Noteworthily, another absolutely new Raman peak at 180.5 cm^{-1} (named as the V_2 mode) appeared and presented a faint red shift with increasing pressure. Simultaneously, two well-resolved Raman peaks of V_1 and v_1 displayed continuous blue shifts until the highest experimental pressure of 48.1 GPa. The corresponding evolution of the Raman shift as a function of pressure for SbI_3 is plotted in Fig. 2d, and the detailed pressure coefficients ($d\omega/dP$) are summarized in Table S1.† It makes clear that the Raman shifts and pressure coefficients of the sample exhibited three prominent inflection points at 3.4, 10.3 and 32.3 GPa, which is probably attributed to the emergence of phase transitions in SbI_3. In addition, the Raman peaks of the sample became asymmetrical with the rise of pressure, which is well illustrated by the symmetric factor. As seen in Fig. S2a,† the v_1 Raman peak is of larger symmetric factor below 8.1 GPa, indicating the higher order of the local structure. Within the pressure range of 8.1–13.5 GPa, the symmetric factor decreased significantly, which is possibly caused by the local structural disorder. However, the obvious enhancement of the symmetric factor above 13.5 GPa is presumably associated with the improved local order with increasing pressure.

Upon depressurization, all of these Raman peaks of the sample monotonically shifted toward lower wavenumbers and the V_2 Raman peak presented progressive weakening, as depicted in Fig. 3. When the pressure was released to 32.6 GPa, the v_3 Raman peak centered at 235.5 cm^{-1} reemerged, concomitance with the disappearance of the V_2 Raman peak. Upon further decompression to 1.2 GPa, the T_z and v_4 Raman peaks of the sample located at 44.6 cm^{-1} and 67.2 cm^{-1} reappeared and an entirely new Raman peak at 75.1 cm^{-1} (designated as the V_3 mode) emerged. Moreover, another new Raman peak at 155.8 cm^{-1} (assigned as the V_4 mode) was identified as the pressure was quenched down to 0.6 GPa. Notably, after the complete release of pressure, the recovered sample presented a different Raman spectrum in comparison with the starting sample, indicating that the decompressed sample cannot transform back to the original rhombohedral SbI_3 phase. Moreover, a conspicuous color transformation from red to black was noticed as the pressure increased from 0.4 GPa to 32.3 GPa (see Fig. S3†), which is a possible manifestation of metallization in pressurized SbI_3, as previously reported in other halides (*e.g.*, BI_3, $SnBr_4$, *etc.*).[30,31] Meanwhile, the very distinct surface color between the pristine and recovered specimens further confirmed the irreversibility of the phase transition.

The evolution of the Raman profiles and Raman shifts with pressure for SbI_3 under hydrostatic condition correlated well with those under non-hydrostatic condition (Fig. S4 and S5†). Specifically, SbI_3 endured three phase transitions at the respective pressures of 2.4, 11.2 and 37.6 GPa under hydrostatic condition. Upon depressurization, the phase transition was found to be irreversible, as proved by the different Raman spectra between the initial and retrieved specimens. In comparison with the transition pressures of SbI_3 under non-hydrostatic condition, we found that the first and second phase transitions occurred at similar pressures under different hydrostatic environments, which is probably related to the feeble deviatoric stress below ~10.0 GPa. As the pressure exceeded ~10.0 GPa, the deviatoric stress was significantly enhanced with increasing pressure under non-hydrostatic condition, whereas a faint enhancement in deviatoric stress was detected under hydrostatic condition, as shown in Fig. S1.† Therefore, the noticeable pressure delay of ~5.0 GPa for the emergence of the third phase transition in SbI_3 under hydrostatic condition is presumably caused by the smaller deviatoric stress, resembling other 2D materials.[12–16,22]

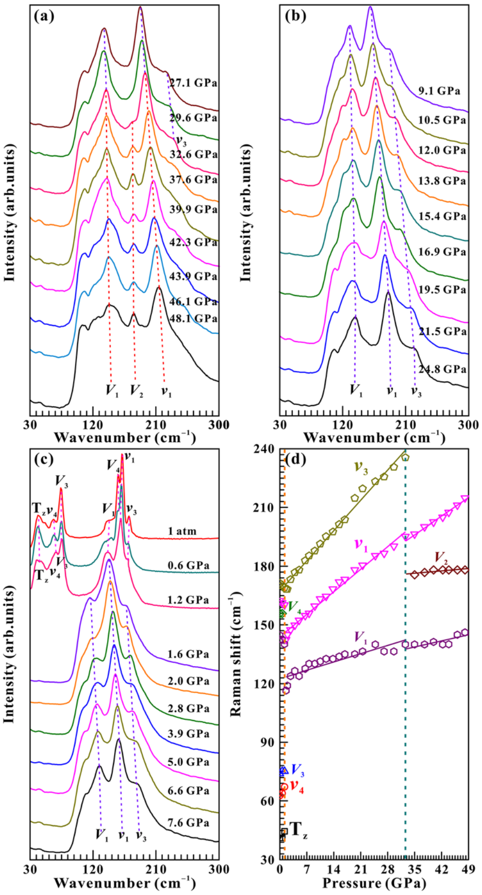

Fig. 3 High-pressure Raman spectra of SbI_3 under non-hydrostatic condition at (a) 48.1–27.1 GPa, (b) 24.8–9.1 GPa, and (c) 7.6–0 GPa. (d) The relationships between Raman shift and pressure at atmospheric temperature during depressurization. Errors in both Raman shifts and pressures are within the size of the symbols.

High-pressure electrical conductivity of SbI_3

Fig. 4 depicts the Nyquist diagrams of the complex impedance spectra for SbI_3 within the pressure range of 0.9–47.1 GPa and room temperature. As seen in Fig. 4a and b, only one available semicircular arc was detectable over the frequency range of 10^{-1}–10^{7} Hz between 0.9 GPa and 22.4 GPa, which corresponds

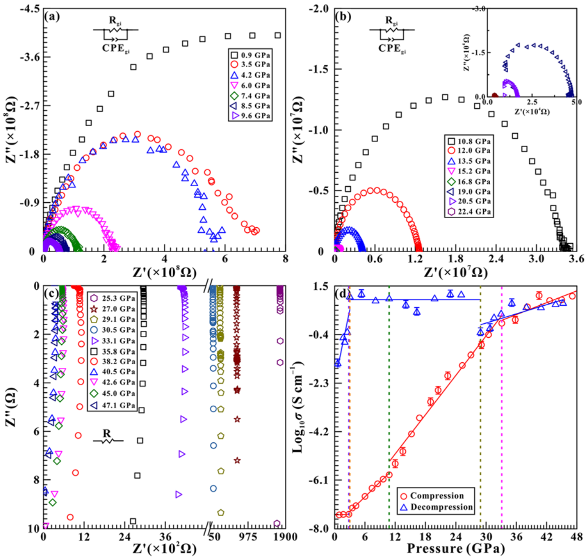

Fig. 4 The Nyquist plots of the complex impedance spectra for SbI_3 at atmospheric temperature and pressure range of (a) 0.9–9.6 GPa, (b) 10.8–22.4 GPa, and (c) 25.3–47.1 GPa, respectively. Herein, Z' and Z'' represent the real and imaginary parts of complex impedance spectroscopy. (d) The corresponding electrical conductivity of SbI_3 as a function of pressure during compression and decompression. Errors in electrical conductivities are within the size of the symbols.

to the grain interior contribution of the sample. Beyond 25.3 GPa, a tilted line perpendicular to the real part of the complex impedance (Z') appeared in the fourth quadrant (see Fig. 4c). The resistance (R) of the sample was determined by fitting the semicircular arc with the equivalent circuit comprising a resistance (R_{gi}) and a constant phase element (CPE_{gi}) in parallel, and the tilted line was fitted by the single resistance (R), respectively. Subsequently, the electrical conductivity (σ) of SbI_3 was calculated using the following formula:

$$\sigma = L/SR \tag{1}$$

where, L denotes the distance between the electrodes (cm), S presents the cross-sectional area of the electrodes (cm^2) and R is the resistance (Ω). Fig. 4d shows the logarithmic electrical conductivity of the sample *versus* pressure at room temperature. It should be noted that the electrical conductivity of SbI_3 is highly susceptible to pressure since a substantial enhancement in electrical conductivity by roughly nine orders of magnitude was discernable as the pressure was elevated from 0.9 GPa to 47.1 GPa. The Bode plots of the complex impedance spectra at 0.9–22.4 GPa is presented in Fig. S6.† Only one relaxation peak belonging to the grain interior was observable, and the relaxation peak moved toward higher frequencies with increasing pressure. Furthermore, we calculated the pressure dependence of the activation energy (dH/dP) for SbI_3 with the following equation, and the corresponding results are listed in Table S2,†

$$d(\ln f)/dP = -1/k_BT(dH/dP) \tag{2}$$

wherein, f is the relaxation frequency, P denotes pressure, k_B is the Boltzmann constant, T stands for temperature and H represents the carrier electrical transport activation energy. It makes clear that the activation energy of the sample decreased with the rise of pressure, suggesting that the transport of the carrier became easier with the occurrence of phase transitions in SbI_3. Taken together, the electrical conductivity and the relaxation frequency presented noticeable discontinuities at 2.8, 10.8 and 33.1 GPa, which are presumably associated with the structural transitions of SbI_3 (Fig. S7†). Importantly, both the high electrical conductivity value of 0.041 S cm^{-1} at 33.1 GPa and the weak dependence of the electrical conductivity on pressure at a feeble rate of 0.078 S cm^{-1} GPa^{-1} are the representative signatures of metallization in SbI_3.[12–16,22] Upon decompression, two prominent inflection points in electrical conductivity at 28.9 GPa and 3.0 GPa were correlated to the reversal of phase transitions, and the unrecoverable electrical conductivity magnitude further validated the irreversibility of the phase transition. Noteworthily, the recovered sample possesses superior electrical transport properties compared to the starting sample with a substantial improvement in the electrical conductivity by six orders of magnitude after pressure treatment, which may inspire the development of high-performance optoelectronic devices in SbI_3.

Variable-temperature electrical conductivity results of SbI_3

Variable-temperature electrical conductivity experiments were conducted to verify the emergence of an electronic transition in pressurized SbI_3 (see Fig. 5 and S8†). Furthermore, the correspondent temperature–pressure–electrical conductivity

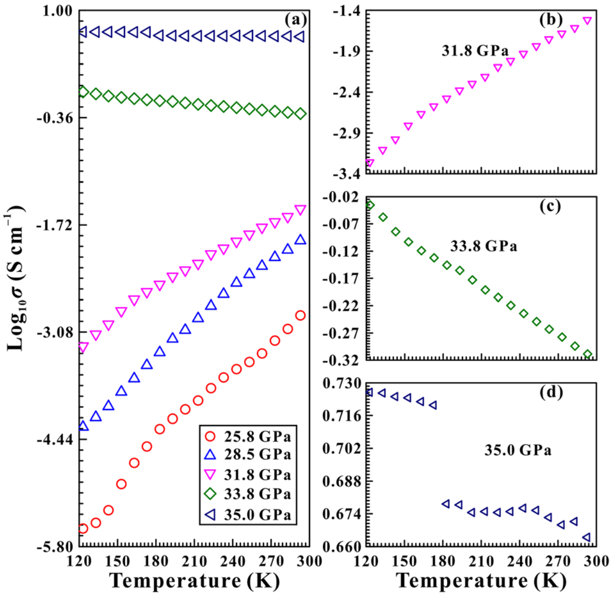

Fig. 5 The variable-temperature electrical conductivity results of SbI_3 at some representative pressures of (a) 25.8, 28.5, 31.8, 33.8 and 35.0 GPa upon compression. (b) The semiconducting feature of the sample at 31.8 GPa. (c and d) The metallic behavior of SbI_3 at 33.8 GPa and 35.0 GPa, respectively.

contour maps were constructed during both processes of compression and decompression (see Fig. 6). According to the solid-state physics theory, a semiconductor has a positive temperature dependence relationship with the electrical conductivity, while a negative temperature dependence relationship with the electrical conductivity is observed for a metal.[12–16,22,32–34] It can be seen from Fig. 5 and 6a that SbI_3 underwent a semiconductor-to-metal transformation as the pressure was enhanced above 33.5 GPa, which was demonstrated by the conversion from positive to negative in the temperature dependence of the electrical conductivity relationship. As illustrated in Fig. 6b and S8,† when the pressure was released below 1.4 GPa, the metallic sample transformed into the semiconducting state since the temperature dependence of the electrical conductivity relationship switched from negative to positive. From the variable-temperature electrical conductivity results, the activation enthalpy of the sample at a fixed pressure can be calculated using the following equation:

$$\sigma = \sigma_0 \exp(-\Delta H / k_B T) \qquad (3)$$

where σ_0 represents the preexponential factor (S m^{-1}), ΔH denotes the activation enthalpy (eV), k_B is the Boltzmann constant and T is the absolute temperature (K), respectively. The activation enthalpy can be obtained by linearly fitting the logarithmic electrical conductivity as a function of $1000/T$. The relationship between the activation enthalpy and pressure is displayed in Fig. S9.† It makes clear that the activation enthalpy decreased with the rise of pressure, making it easier for charge carriers to jump across the potential barrier. More importantly, the activation enthalpy of the sample was reduced to zero at 33.8 GPa, which suggested the disappearance of the energy barrier. In other words, SbI_3 exhibits the metallic property above 33.8 GPa.

First-principles theoretical calculations of SbI_3

To elucidate the occurrence of high-pressure structural transitions in SbI_3, first-principles theoretical calculations were implemented at 0–50.0 GPa. As illustrated in Fig. 7a, the $R\bar{3}$ structural phase has lower enthalpy below 35.0 GPa, indicating its structural stability. Notably, the $C2/m$ structural phase possessed lower enthalpy above 35.0 GPa, which suggested that the $R\bar{3}$ structural phase was transformed into the $C2/m$ structural phase at 35.0 GPa. Meanwhile, some characteristic crystalline parameters of SbI_3, including the lattice constants (a, b and c), lattice constant ratios (a/c, a/b and b/c), normalized lattice constants (a/a_0, b/b_0 and c/c_0), unit cell volume (V) and Sb–I bond length under high pressure were acquired and are presented in Fig. 7b–f. Notably, the prominent discontinuities in all of these fitting parameters including the pressure-dependent a, b, c, a/b, a/c, b/c, a/a_0, b/b_0, c/c_0, V and Sb–I bond length were observable at 35.0 GPa, which revealed that SbI_3 possibly underwent a structural transformation. More specifically, the c, a/c (b/c), c/c_0 and Sb–I bond length presented two obvious inflection points at the respective pressures of 3.0 GPa and 10.0 GPa within the pressure range of 0–15.0 GPa, as illustrated in detail in Fig. 8. In fact, the IPTs for some representative binary compounds (*e.g.*, $CrCl_3$, $CrBr_3$, Bi_2S_3, Sb_2S_3, Sb_2Se_3, VSe_2, *etc.*) are characterized by the striking inflection point in the lattice constant ratio.[22,35–39] Therefore, the first and second phase transitions of SbI_3 possibly belong to the IPTs resulting from the prominent compression of the c-axis and Sb–I bond under high pressure, while the third phase transition presumably originates from the $R\bar{3}$-to-$C2/m$ structural transition. Moreover, the crystalline structures and the detailed atomic positions of SbI_3 at four characteristic pressures of 0, 3.0, 10.0 and 35.0 GPa are displayed in Fig. S10 and Table S3,† respectively.

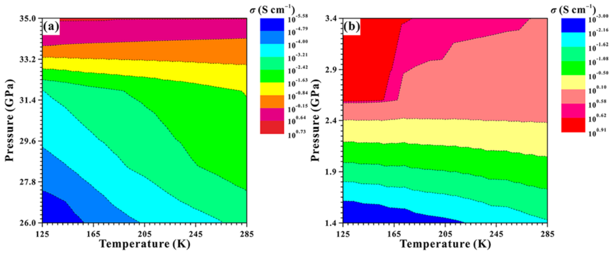

Fig. 6 Temperature–pressure–electrical conductivity contour maps of SbI_3 during (a) pressurization and (b) depressurization, respectively.

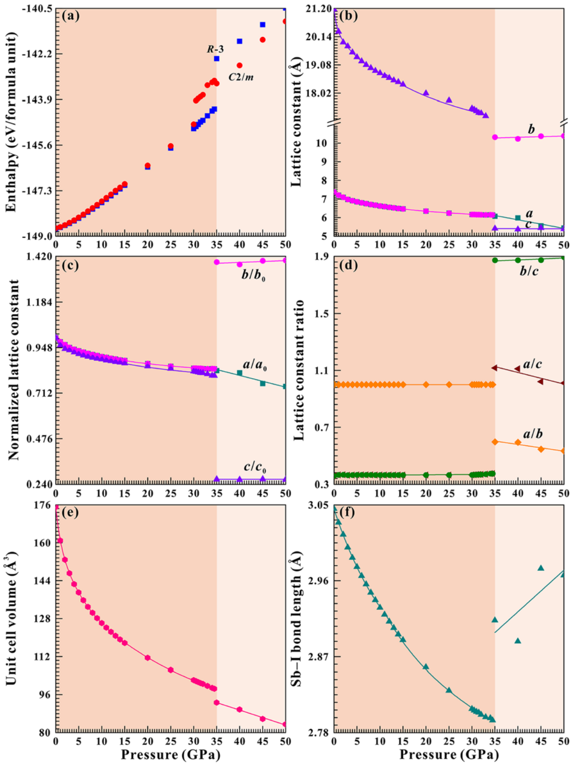

Fig. 7 Calculated (a) enthalpy, (b) lattice constants, (c) normalized lattice constants, (d) lattice constant ratios, (e) unit cell volume, and (f) Sb–I bond length for SbI_3 at 0–50.0 GPa.

The electronic band structures and their corresponding density of states for SbI_3 under high pressure were calculated and are presented in Fig. 9. At ambient conditions, the initial

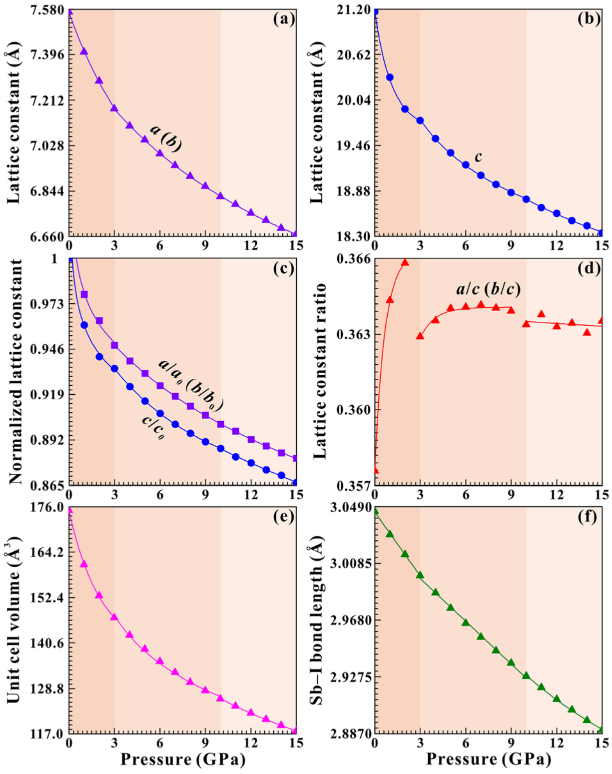

Fig. 8 Theoretical calculation results on (a) and (b) lattice constants, (c) normalized lattice constants, (d) lattice constant ratios, (e) unit cell volume, and (f) Sb–I bond length for SbI_3 within the pressure range of 0–15.0 GPa.

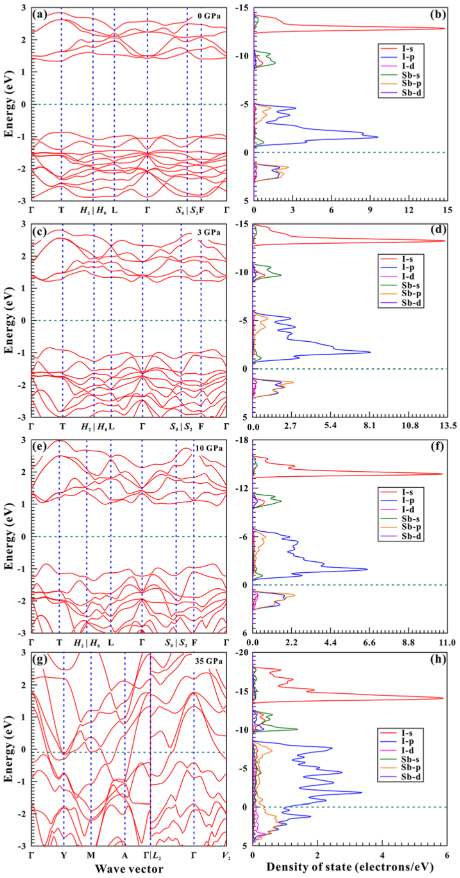

Fig. 9 Calculated electronic band structures (a, c, e, and g) and their correspondent density of states (b, d, f, and h) for SbI_3 at four typical pressures of 0, 3.0, 10.0, and 35.0 GPa, respectively. The bandgap energies of (a, c, e, and g) are 2.21, 2.04, 1.80, and 0 eV, respectively.

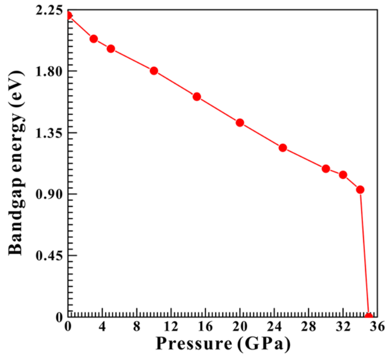

Fig. 10 The evolution of the bandgap energy as a function of pressure for SbI_3 within a broad pressure range of 0–35.0 GPa from first-principles theoretical calculations.

$R\bar{3}$ structural phase belongs to a wide bandgap semiconductor with the direct bandgap energy of 2.21 eV, which is consistent with previous theoretical calculation results.[10,11,18] With the rise of pressure, both valence and conduction bands for the $R\bar{3}$ structural phase moved towards the Fermi level, indicating that the bandgap gradually becomes narrow. The detailed evolution of the bandgap energy under high pressure is presented in Fig. 10. Below 34.0 GPa, the bandgap energy of the $R\bar{3}$ structural phase gradually decreased with the rise of pressure. Notably, upon further compression to 35.0 GPa, the valence and conduction bands of the $C2/m$ structural phase crossed the Fermi level, manifesting the metallic property. Therefore, our theoretical calculation results suggested that the metallization of SbI_3 is induced by the $R\bar{3}$-to-$C2/m$ structural transition under high pressure.

Synchrotron X-ray diffraction of SbI_3

To further confirm the occurrence of pressure-driven structural transitions, we performed the synchrotron X-ray diffraction experiments on SbI_3 at four representative pressures of 1.5, 8.0, 20.0 and 40.0 GPa under non-hydrostatic condition. The high-pressure synchrotron XRD patterns of SbI_3 and their corresponding refinement results are illustrated in Fig. 11 and 12 and summarized in Table S4,† respectively. In Fig. 11, as one example of our acquired XRD pattern of SbI_3 at the pressure of 1.5 GPa by virtue of a diamond anvil cell, it is extremely analogous to a previously available result reported by Hsueh *et al.* (1998) at 1.6 GPa.[9] The synchrotron X-ray diffraction peak of SbI_3 was identified as the initial rhombohedral structure ($R\bar{3}$) with its corresponding lattice parameters of $a = b = 7.113 \pm 0.002$ Å, $c = 19.293 \pm 0.009$ Å, $\alpha = \beta = 90°$, $\gamma = 120°$,

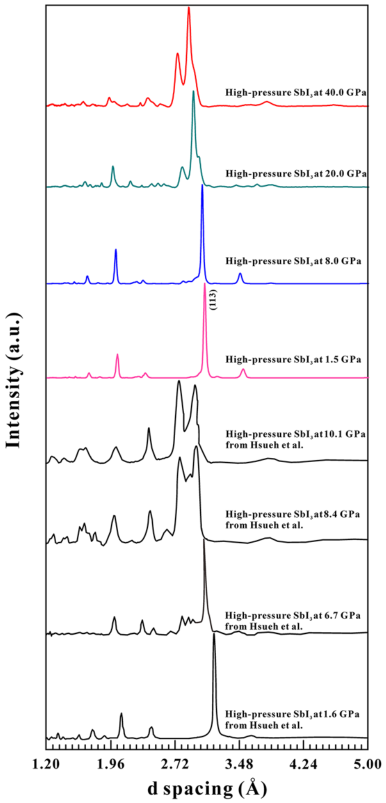

Fig. 11 The typical X-ray diffraction patterns of SbI_3 at the representative pressures of 1.5, 8.0, 20.0, and 40.0 GPa under non-hydrostatic condition. Previously reported X-ray diffraction results on SbI_3 at 1.6, 6.7, 8.4, and 10.1 GPa under non-hydrostatic condition are also compared in detail.

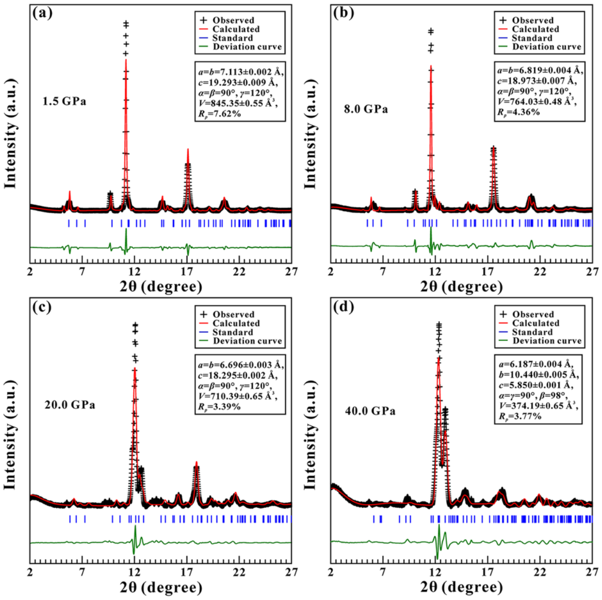

Fig. 12 Rietveld refinement results of the synchrotron X-ray diffraction patterns for SbI_3 at (a) 1.5 GPa, (b) 8.0 GPa, (c) 20.0 GPa, and (d) 40.0 GPa. Herein, the experimental and calculated patterns are indicated by the black cross symbols and the red solid lines, respectively. The green solid lines at the bottom are the deviation curves between the observed and calculated profiles. The vertical blue bars represent the standard positions of the Bragg peaks.

and V = 845.35 ± 0.55 Å^3 at the pressure of 1.5 GPa, respectively. As the pressure increased to 8.0 GPa, the XRD peaks of SbI_3 shifted towards the lower d spacing values and implied the unit cell to be compressed, which accords well with our theoretical calculation results under high pressure. Concurrently, the (113) predominant peak asymmetrically broadened, which was accompanied by the emergence and disappearance of several feeble peaks around the dominant pattern. Furthermore, the XRD pattern at 8.0 GPa was affirmed as the rhombohedral structure ($R\bar{3}$) with its corresponding lattice parameters of a = b = 6.819 ± 0.004 Å, c = 18.973 ± 0.007 Å, $\alpha = \beta = 90°$, $\gamma = 120°$, and V = 764.03 ± 0.48 Å^3, respectively. As the pressure approached 20.0 GPa, it is clear that two obviously available shoulder peaks were observed along the (113) characteristic pattern, which was indexed as the rhombohedral structure ($R\bar{3}$) with its corresponding lattice parameters of a = b = 6.696 ± 0.003 Å, c = 18.295 ± 0.002 Å, $\alpha = \beta = 90°$, $\gamma = 120°$, and V = 710.39 ± 0.65 Å^3, respectively. Upon compression to 40.0 GPa, the main peak was split into two separate peaks with the high intensities, and the diffraction pattern was further identified as the monoclinic structure ($C2/m$) with its corresponding lattice parameters of a = 6.187 ± 0.004 Å, b = 10.440 ± 0.005 Å, c = 5.850 ± 0.001 Å, $\alpha = \gamma = 90°$, $\beta = 98°$, and V = 374.19 ± 0.65 Å^3, respectively. Previously reported synchrotron XRD results in SbI_3 by Hsueh *et al.* were measured under four limited pressures of 1.6 GPa, 6.7 GPa, 8.4 GPa and 10.1 GPa. Furthermore, a structural transformation from the rhombohedral ($R\bar{3}$) to monoclinic ($P2_1/c$) phases was extrapolated beyond 4.0 GPa. It should be noted that the high-pressure synchrotron XRD patterns of SbI_3 above ∼8.0 GPa reported by Hsueh *et al.* and us are completely different. Three possible causes were proposed to explain the inconsistent XRD profiles above ∼8.0 GPa as follows: (i) the inevitable influence of the pressure scale on the synchrotron X-ray diffraction pattern. Although both Hsueh *et al.* and our high-pressure synchrotron XRD experiments were performed without pressure medium under non-hydrostatic condition, we chose both gold and ruby as the pressure scale in the present work (Fig. S11†), while only ruby was employed to calibrate the pressure in previous study. And thus, it is possibly inevitable that the discrepancy in pressure scale may influence the synchrotron XRD signal of sample; (ii) the divergence of starting samples, which may lead to the available discrepancy in the high-pressure structural behaviors of SbI_3. In this work, the polycrystalline SbI_3 aggregates with their correspondent grain size of 1–3 μm were obtained from Leshan Kairuida Photoelectric Technology Company, which were sealed into the sample chamber of a diamond anvil cell. In a previous study, the starting SbI_3 samples were purchased from the Alfa Company without further purification, which were ground into fine powders to minimize the effects of preferred orientation and loaded into a diamond anvil cell. The similar discrepancy phenomena in high-pressure synchrotron XRD results caused by the divergence of starting samples, such as VSe_2, HfS_2, $HfTe_3$, *etc.*, were also observed in other previously reported two-dimensional layered compounds;[38,40,41] (iii) the inconsistent XRD profiles beyond ~8.0 GPa corresponding to different high-pressure structural phases of SbI_3. In our present study, the asymmetrically broad (113) predominant peak and the emergence and disappearance of several feeble peaks in the synchrotron XRD pattern revealed an IPT within the pressure range of 8.0 GPa and 20.0 GPa, which still retained the initial high-pressure rhombohedral ($R\bar{3}$) structural phase of SbI_3. Upon pressurization to 40.0 GPa, the splitting of the main peak in SbI_3 was characterized by the new phase of the monoclinic $C2/m$ sample. In conclusion, all of these observed high-pressure synchrotron XRD results on SbI_3 were in good agreement with our above-mentioned first-principles theoretical calculations, electrical conductivity and Raman spectroscopy data under high pressure.

Previous Raman spectra results on SbI_3 demonstrated the occurrence of IPT by the inversion from a red shift to blue shift in Raman peaks at around the transition pressure.[9,17] In fact, we have also observed the similar Raman scattering phenomenon of the initial softening followed by the hardening for Raman peaks at 3.4 GPa. Consequently, the structural transition at 3.4 GPa was presumably attributed to the IPT, which matches well with our theoretical calculation results. As for the second phase transition of SbI_3 at 10.3 GPa, our obtained transition pressure is comparable to that of 8.3 GPa from previous Raman scattering results reported by Anderson *et al.* (1998).[17] Notably, the metallization at 32.3 GPa is induced by the $R\bar{3}$-to-$C2/m$ structural transformation, which is totally different from previously theoretical calculation results under high pressure.[18] During decompression, the irreversibility of structural transition was also revealed from earlier synchrotron X-ray diffraction and Raman spectroscopy results, which was possibly ascribed to the huge kinetic barrier for the continuous high-pressure structural transitions of SbI_3.[9,17]

As the typical members of the VA group metal triiodide, BiI_3 and SbI_3 share analogous electronic structures at ambient conditions.[9] Recently, BiI_3 has been reported to undergo a semiconductor-to-metal transformation at ~35.0 GPa by means of optical absorption measurements under quasi-hydrostatic condition using CsI powder as the PM.[42] In the present work, both Raman scattering and electrical conductivity results disclosed the occurrence of an electronic transition in SbI_3 at 32.3 GPa under non-hydrostatic condition. Nevertheless, SbI_3 metallizes at higher pressure of 37.6 GPa under hydrostatic condition using helium as the PM. The slightly lower metallization pressure of SbI_3 relative to BiI_3 possibly derives from the following causes. On the one hand, the narrower electronic orbitals of antimony than that of bismuth led to the mildly weaker hybridization of 5p and 5d orbitals in SbI_3 than the 5p and 6d orbitals in BiI_3. Actually, a similar trend of metallization pressure has also been reported in transition-metal dichalcogenides (TMDs, MX_2) (M = Mo and W; X = S and Se).[43–45] On the other hand, previous high-pressure investigations on some representative 2D compounds have demonstrated that the degree of hydrostaticity is a crucial factor of influencing the structural and electronic transition pressures under different hydrostatic environments.[12–16,22] Consequently, the lower metallization pressure of SbI_3 in comparison with BiI_3 may be associated with the absence of PM, which could accelerate the emergence of metallization under non-hydrostatic condition.

Conclusions

In the present work, the crystalline structure and electrical transport properties of quasimolecular layered SbI_3 during compression and decompression under different hydrostatic environments have been comprehensively studied through *in situ* synchrotron X-ray diffraction, Raman spectroscopy, electrical conductivity in combination with first-principles theoretical calculations. Under non-hydrostatic condition, SbI_3 experienced two IPTs at the respective pressures of 3.4 GPa and 10.3 GPa, followed by a metallization at 32.3 GPa. Nevertheless, SbI_3 metallized at higher pressure of 37.6 GPa under hydrostatic condition due to the feeble deviatoric stress. Upon depressurization, the phase transition of SbI_3 was found to be irreversible under different hydrostatic environments.

Author contributions

Lidong Dai and Haiying Hu performed the conceptualization of this article and led the project. Meiling Hong and Xinyu Zhang performed the investigation including XRD, high-pressure Raman spectra and high-pressure electrical conductivity measurements. Xiaolei Feng and Shidong Yu performed first-principles theoretical calculations. Limin Zhang and Zhongying Mi performed the synchrotron X-ray diffraction and analysed the results. Meiling Hong, Lidong Dai and Sivakumar Aswathappa contributed to the analysis, interpretation and discussion of these results. Meiling Hong and Lidong Dai performed the writing – original draft. Meiling Hong, Lidong Dai, Haiying Hu, Xinyu Zhang and Chuang Li performed the writing – review & editing. All authors commented on the final manuscript. Lidong Dai and Haiying Hu supervised the project.

Conflicts of interest

There are no conflicts to declare.

Acknowledgements

We thank Professor Jun Chen and two anonymous reviewers for their very helpful comments and suggestions in the reviewing process, which helped us greatly in improving the manuscript. The authors acknowledge the technical support of the *in situ* high-pressure Raman scattering measurements provided by Professor Heping Li in the Key Laboratory of High-

Temperature and High-Pressure Study of the Earth's Interior, Institute of Geochemistry, Chinese Academy of Sciences. This research was financially supported by the NSF of China (grant numbers 42072055, 42274137 and 42302047). In addition, high-pressure synchrotron X-ray diffraction measurements and the theoretical calculation results were performed on Beijing Synchrotron Radiation Facility (BSRF) and National Supercomputing Centre (NSCC), Singapore (**https://www.nscc.sg**), respectively.

References

1 M. Kępińska, M. Nowak, P. Duka, M. Kotyczka-Morańska and P. Szperlich, Optical properties of SbI_3 single crystalline platelets, *Opt. Mater.*, 2011, **33**, 1753–1759.

2 M. Kępińska, A. Starczewska, I. Bednarczyk, J. Szala, P. Szperlich and K. Mistewicz, Fabrication and characterisation of SbI_3-opal structures, *Mater. Lett.*, 2014, **130**, 17–20.

3 M. H. Chen and L. Gao, Polyol method synthesis and characterization of nanoscale Sb_2Se_3 wires, *Mater. Res. Bull.*, 2005, **40**, 1120–1125.

4 T. Onodera, K. Baba and K. Hitomi, Evaluation of antimony tri-iodide crystals for radiation detectors, *Sci. Technol. Nucl. Install.*, 2018, **2018**, 1532742.

5 D. B. Mohan, A. Philip and C. S. Sunandana, Iodization of antimony thin films: XRD, SEM and optical studies of nanostructured SbI_3, *Vacuum*, 2008, **82**, 561–565.

6 A. A. Ramachandran, B. Krishnan, S. Devasia, D. A. Avellaneda, M. I. M. Palma, J. A. A. Martinez and S. Shaji, Photosensitive antimony triiodide thin films by rapid iodization of chemically deposited antimony sulfide, *Mater. Res. Bull.*, 2021, **142**, 111382.

7 A. Saiton, T. Komatsu, T. Karasawa, H. Ohtake and T. Suemoto, Raman scattering under hydrostatic pressures in layered BiI_3 and SbI_3 crystals, *Phys. Status Solidi B*, 2001, **226**, 357–367.

8 A. Saitoh, Raman scattering, luminescence, and absorption edge under hydrostatic pressures of layered BiI_3 and SbI_3, *J. Raman Spectrosc.*, 2007, **38**, 537–542.

9 H. C. Hsueh, R. K. Chen, H. Vass, S. J. Clark, G. J. Ackland, C.-K. Poon and J. Crain, Compression mechanisms in quasimolecular XI_3 (X = As, Sb, Bi) solids, *Phys. Rev. B: Condens. Matter Mater. Phys.*, 1998, **58**, 14812.

10 K. Lai, C.-L. Yan, L.-Q. Gao and W.-B. Zhang, AI_3 (A = As, Sb) single-layers and their vdW heterostructure for photocatalysis and solar cell applications, *J. Phys. Chem. C*, 2018, **122**, 7656–7663.

11 P. Liu, F. Lu, M. K. Wu, X. G. Luo, Y. H. Cheng, X.-W. Wang, W. C. Wang, W.-H. Wang, H. Liu and K. Cho, Electronic structures and band alignments of monolayer metal trihalide semiconductors MX_3, *J. Mater. Chem. C*, 2017, **5**, 9066–9071.

12 Y. K. Zhuang, L. D. Dai, L. Wu, H. P. Li, H. Y. Hu, K. X. Liu, L. F. Yang and C. Pu, Pressure-induced permanent metallization with reversible structural transition in molybdenum disulfide, *Appl. Phys. Lett.*, 2017, **110**, 122103.

13 Y. K. Zhuang, L. D. Dai, H. P. Li, H. Y. Hu, K. X. Liu, L. F. Yang, C. Pu, M. L. Hong and P. F. Liu, Deviatoric stresses promoted metallization in rhenium disulfide, *J. Phys. D: Appl. Phys.*, 2018, **51**, 165101.

14 M. L. Hong, L. D. Dai, H. Y. Hu, X. Y. Zhang, C. Li and Y. He, Pressure-induced structural phase transition and metallization of $CrCl_3$ under different hydrostatic environments up to 50.0 GPa, *Inorg. Chem.*, 2022, **61**, 4852–4864.

15 M. L. Hong, L. D. Dai, H. Y. Hu, X. Y. Zhang, C. Li and Y. He, High-pressure structural phase transitions and metallization in layered HfS_2 under different hydrostatic environments up to 42.1 GPa, *J. Mater. Chem. C*, 2022, **10**, 10541–10550.

16 X. Y. Zhang, L. D. Dai, H. Y. Hu, M. L. Hong and C. Li, Pressure-induced coupled structural-electronic transition in SnS_2 under different hydrostatic environments up to 39.7 GPa, *RSC Adv.*, 2022, **12**, 2454–2461.

17 A. Anderson, S. K. Sharma, S. Y. Wang and Z. Wang, Raman study of antimony triiodide at high pressures, *J. Raman Spectrosc.*, 1998, **29**, 251–255.

18 X.-X. Sun, C. Li, Q.-Y. Hou and Y. Zhang, Phase transition and electronic properties of SbI_3: First-principles calculations, *Mod. Phys. Lett. B*, 2017, **31**, 1750200.

19 S. Klotz, J.-C. Chervin, P. Munsch and G. Le Marchand, Hydrostatic limits of 11 pressure transmitting media, *J. Phys. D: Appl. Phys.*, 2009, **42**, 075413.

20 A. Celeste, F. Borondics and F. Capitani, Hydrostaticity of pressure-transmitting media for high pressure infrared spectroscopy, *High Pressure Res.*, 2019, **39**, 608–618.

21 K. Takemura, Hydrostaticity in high pressure experiments: some general observations and guidelines for high pressure experiments, *High Pressure Res.*, 2021, **41**, 155–174.

22 M. L. Hong, L. D. Dai, H. Y. Hu, X. Y. Zhang, C. Li and Y. He, Pressure-driven structural phase transitions and metallization in the two-dimensional ferromagnetic semiconductor $CrBr_3$, *Dalton Trans.*, 2023, **52**, 7290–7301.

23 M. Q. Xiao, H. Yang, W. F. Shen, C. G. Hu, K. Zhao, Q. Gao, L. F. Pan, L. Y. Liu, C. L. Wang, G. Z. Shen, H.-X. Deng, H. Y. Wen and Z. M. Wei, Symmetry-reduction enhanced polarization-sensitive photodetection in core-shell SbI_3/Sb_2O_3 van der Waals heterostructure, *Small*, 2020, **16**, 1907172.

24 X. X. Sun, C. L. Wu, W. W. Chen and H. S. Liu, Structural and elastic properties of antimony triiodide from first-principles calculations, *Adv. Mater. Res.*, 2013, **750**, 1782–1785.

25 A. C. Larson and R. B. Von Dreele, General structure analysis system (GSAS), Los Alamos National Laboratory Report LAUR 86-748, 2005.

26 G. Kresse and J. Furthmüller, Efficient iterative schemes for *ab initio* total-energy calculations using a plane-wave basis set, *Phys. Rev. B: Condens. Matter Mater. Phys.*, 1996, **54**, 11169–11186.

27 P. E. Blöchl, Projector augmented-wave method, *Phys. Rev. B: Condens. Matter Mater. Phys.*, 1994, **50**, 17953–17979.

28 G. Kresse and D. Joubert, From ultrasoft pseudopotentials to the projector augmented-wave method, *Phys. Rev. B: Condens. Matter Mater. Phys.*, 1999, **59**, 1758–1775.

29 J. W. Sun, A. Ruzsinszky and J. P. Perdew, Strongly constrained and appropriately normed semilocal density functional, *Phys. Rev. Lett.*, 2015, **115**, 036402.

30 X. L. Huang, D. F. Duan, K. Wang, X. Y. Yang, S. Q. Jiang, W. B. Li, F. F. Li, Q. Zhou, X. L. Jin, B. Zou, B. B. Liu and T. Cui, Structural and electronic changes of $SnBr_4$ under high pressure, *J. Phys. Chem. C*, 2013, **117**, 8381–8387.

31 N. Hamaya, M. Ishizuka, S. Onoda, J. Guishan, A. Ohmura and K. Shimizu, Pressure-induced phase transition, metallization, and superconductivity in boron triiodide, *Phys. Rev. B: Condens. Matter Mater. Phys.*, 2010, **82**, 094506.

32 L. D. Dai, K. X. Liu, H. P. Li, L. Wu, H. Y. Hu, Y. K. Zhuang, L. F. Yang, C. Pu and P. F. Liu, Pressure-induced irreversible metallization accompanying the phase transitions in Sb_2S_3, *Phys. Rev. B*, 2018, **97**, 024103.

33 L. F. Yang, J. J. Jiang, L. D. Dai, H. Y. Hu, M. L. Hong, X. Y. Zhang, H. P. Li and P. F. Liu, High-pressure structural phase transition and metallization in Ga_2S_3 under non-hydrostatic and hydrostatic conditions up to 36.4 GPa, *J. Mater. Chem. C*, 2021, **9**, 2912–2918.

34 L. D. Dai, C. Pu, H. P. Li, H. Y. Hu, K. X. Liu, L. F. Yang and M. L. Hong, Characterization of metallization and amorphization for GaP under different hydrostatic environments in diamond anvil cell up to 40.0 GPa, *Rev. Sci. Instrum.*, 2019, **90**, 066103.

35 A. S. Ahmad, Y. C. Liang, M. D. Dong, X. F. Zhou, L. M. Fang, Y. H. Xia, J. H. Dai, X. Z. Yan, X. H. Yu, J. F. Dai, G. J. Zhang, W. Q. Zhang, Y. S. Zhao and S. M. Wang, Pressure-driven switching of magnetism in layered $CrCl_3$, *Nanoscale*, 2020, **12**, 22935–22944.

36 C. Y. Li, J. G. Zhao, Q. Y. Hu, Z. G. Liu, Z. H. Yu and H. Yan, Crystal structure and transporting properties of Bi_2S_3 under high pressure: Experimental and theoretical studies, *J. Alloys Compd.*, 2016, **688**, 329–335.

37 I. Efthimiopoulos, C. Buchan and Y. J. Wang, Structural properties of Sb_2S_3 under pressure: evidence of an electronic topological transition, *Sci. Rep.*, 2016, **6**, 24246.

38 S. Pal, K. Debnath, S. N. Gupta, L. Harnagea, D. V. S. Muthu, U. V. Waghmare and A. K. Sood, Pressure-induced 1*T* to 3*R* structural phase transition in metallic VSe_2: X-ray diffraction and first-principles theory, *Phys. Rev. B*, 2021, **104**, 014108.

39 I. Efthimiopoulos, J. M. Zhang, M. Kucway, C. K. Park, R. C. Ewing and Y. J. Wang, Sb_2Se_3 under high pressure, *Sci. Rep.*, 2013, **3**, 2665.

40 W. Zhong, W. Deng, F. Hong and B. B. Yue, Structural and electronic phase transition in the van der Waals crystal HfS_2 under high pressure, *Phys. Rev. B*, 2023, **107**, 134118.

41 J. Li, J. Peng, S. Zhang and G. F. Chen, Anisotropic multichain nature and filamentary superconductivity in the charge density wave system $HfTe_3$, *Phys. Rev. B*, 2017, **96**, 174510.

42 U. Schwarz, A. Wosylus, M. Schmidt, L. Akselrud, A. Ormeci, M. Hanfland, V. Hermann and C. Kuntscher, High-pressure modification of BiI_3, *Inorganics*, 2019, **7**, 143.

43 Z. Zhao, H. J. Zhang, H. T. Yuan, S. B. Wang, Y. Lin, Q. S. Zeng, G. Xu, Z. X. Liu, G. K. Solanki, K. D. Patel, Y. Cui, H. Y. Hwang and W. L. Mao, Pressure induced metallization with absence of structural transition in layered molybdenum diselenide, *Nat. Commun.*, 2015, **6**, 7312.

44 P. F. Shen, X. Ma, Z. Guan, Q. J. Li, H. F. Zhang, R. Liu, B. Liu, X. G. Yang, Q. Dong, T. Cui and B. B. Liu, Linear tunability of the band gap and two-dimensional (2D) to three-dimensional (3D) isostructural transition in WSe_2 under high pressure, *J. Phys. Chem. C*, 2017, **121**, 26019–26026.

45 Y. B. Gong, Q. Zhou, Y. Liu, X. P. Fu, M. G. Yao, X. L. Huang, Y. P. Huang, H. X. Gao, F. F. Li and T. Cui, Increasing interlayer coupling prevented the deformation in compressed multilayer WSe_2, *J. Phys. Chem. C*, 2018, **122**, 10261–10266.